

In Situ Analysis of Europium Calcium Oxalate Crystallization Using Luminescence Microspectroscopy

Michael J. Lochhead

Department of Chemical Engineering, University of New Hampshire, Durham, New Hampshire 03824

Lara Touryan and Viola Vogel*

Department of Bioengineering, University of Washington, Seattle, Washington 98195

Received: November 5, 1998; In Final Form: February 22, 1999

Luminescence microspectroscopy (LMS) is described here as an in situ approach that combines the spatial resolution and imaging capabilities of optical microscopy with the structural sensitivity of rare earth ion spectroscopy. In this work, LMS, laser-induced luminescence spectroscopy, and conventional Raman spectroscopy were used to analyze the effect of Eu^{3+} admixtures on calcium oxalate crystallization. This new combination of techniques was used to establish a link between crystal morphology, phase, and impurity ion bonding environments for single crystals in contact with their aqueous growth solution. Distinct, spatially resolved Eu^{3+} luminescence spectra were measured for 1–20 μm crystals separated by less than 10 μm . Results show that micromolar quantities of Eu^{3+} significantly inhibit calcium oxalate nucleation in static, low ionic strength (~ 2 mM) supersaturated solutions at room temperature. Eu^{3+} stabilizes and incorporates into the dihydrate phase of calcium oxalate and the bipyramidal morphology associated with this phase is maintained. Eu^{3+} is believed to occupy Ca^{2+} lattice sites in the dihydrate crystals. Eu^{3+} also associates with calcium oxalate monohydrate during crystallization, yielding several ill-formed crystal morphologies. Two classes of Eu^{3+} bonding environments are identified in the monohydrate, including one with unusual luminescence band energies. The luminescence spectra are interpreted in terms of the local structure of the calcium oxalate crystal lattices. These experiments demonstrate LMS to be a useful approach for a spatially controlled analysis of inorganic crystal growth at surfaces in real time. Potential applications include analysis of template-directed crystallization, biomineralization, phosphors, and ceramic coatings.

Introduction

The controlled nucleation and growth of ionic crystals is of major significance in systems ranging from industrial processes¹ to natural biomineralization.² Both in the industrial setting and in nature, admixtures in the system greatly influence crystal size, morphology, and phase. Improved control over crystal nucleation and growth will rely on an improved molecular understanding of how admixtures, both desired (additives) and undesired (impurities), alter crystallization. In an effort to provide new insight into the molecular mechanisms of admixture incorporation, we use an in situ approach that directly probes metal ion local structure during crystal growth. The technique, called luminescence microspectroscopy (LMS), combines the spatial resolution of optical microscopy with the structural sensitivity of rare earth ion spectroscopy and allows real time measurements while crystals are in contact with their aqueous growth solution. It is used here to investigate crystal formation in the europium–calcium-oxalate system ($\text{Eu}:\text{CaC}_2\text{O}_4$).

Interest in the microscopic nucleation and growth of CaC_2O_4 stems in part from its importance as a biomineral; it is the primary mineral constituent in most human kidney stones³ and is found in numerous plant species.⁴ Adding trace amounts of

Eu^{3+} to this system provides insight into how metal ion impurities alter CaC_2O_4 nucleation and growth. At the same time, Eu^{3+} serves as a luminescent probe of local structure, since the ion has spectral properties sensitive to its local bonding environment.⁵ In addition, $\text{Eu}:\text{CaC}_2\text{O}_4$ itself is significant, since oxalic acid precipitation is commonly used to purify the rare earth ions from other metal cations.⁶

Results are presented for low ionic strength (~ 2 mM) batch crystallizations showing that micromolar quantities of Eu^{3+} significantly alter CaC_2O_4 nucleation kinetics, phase, and crystal morphology relative to solutions containing no admixtures. Growth of Eu^{3+} -containing CaC_2O_4 crystals is analyzed, and crystal structure is linked to crystal morphology through LMS and Raman spectroscopy.

The combination of techniques used in this research represents a new direction in the study of interfacial crystallization phenomena. Traditional spectroscopy measurements are typically performed after samples are removed from their aqueous growth solutions and often result in averaged data representing contributions from an ensemble of crystals. Linking these averaged data with molecular structure and growth mechanisms is often difficult. The experiments described in this paper allow spectra to be collected from micrometer-scale single crystals still in contact with their growth solution. Single crystal and surface-specific spectral measurements promise to provide new molecular-level insight into mineralization phenomena.

* Corresponding author. Department of Bioengineering, Box 352125, University of Washington, Seattle, WA 98195. Email: vogel@bioeng.washington.edu.

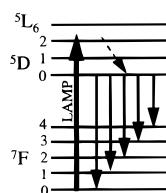


Figure 1. Simplified energy level diagram for Eu^{3+} .

Theory: Eu^{3+} Spectroscopy

The trivalent Eu^{3+} ion has been used extensively as a luminescent structural probe.⁵ This section briefly reviews features of Eu^{3+} that make it attractive spectroscopically. Readers are referred to the Bünzli and Choppin book⁵ for a more thorough description and review of the literature.

Figure 1 shows a simplified energy level diagram of Eu^{3+} . Eu^{3+} has a $[\text{Xe}]4f^6$ electronic configuration and the arrows indicate the intraconfigurational $f-f$ transitions in the visible part of the spectrum. Electron shielding of the f orbitals in Eu^{3+} leads to relatively narrow absorption and emission bands, even at room temperature. Because these transitions are all forbidden by the Laporte (parity) selection rule, their intensities are generally low. Interaction with the ligand field, however, mixes opposite parity states into the $4f$ wave functions and transitions are observable with intensities and energies sensitive to the local bonding environment around the ion. The $^5\text{D}_0 \rightarrow ^7\text{F}_0$ transition is of particular interest because both states involved in the transition are nondegenerate. Consequently, any splitting or broadening observed in this band is indicative of a distribution of dissimilar Eu^{3+} bonding sites.

In our experiments we use a xenon lamp and filter combination to excite the $^7\text{F}_0 \rightarrow ^5\text{L}_6$, $^5\text{D}_2$, and $^5\text{D}_1$ absorption bands of Eu^{3+} , centered at approximately 394, 465, and 530 nm, respectively. We also use the 514.5 nm line of an argon laser to excite the high-energy edge of the $^5\text{D}_0 \rightarrow ^7\text{F}_1$ absorption. In our samples, rapid nonradiative decay from the higher excited states to the $^5\text{D}_0$ state occurs, and the luminescence spectra are dominated by the $^5\text{D}_0 \rightarrow ^7\text{F}_0$ (~ 580 nm), $^5\text{D}_0 \rightarrow ^7\text{F}_1$ (~ 590 nm), $^5\text{D}_0 \rightarrow ^7\text{F}_2$ (610–620 nm), $^5\text{D}_0 \rightarrow ^7\text{F}_3$ (weak, ~ 650 nm), and $^5\text{D}_0 \rightarrow ^7\text{F}_4$ (~ 680 –710 nm) emission bands.

It is important to note that because of their high vibrational energy, hydroxyl groups coordinating Eu^{3+} efficiently quench Eu^{3+} luminescence.⁷ At the low Eu^{3+} concentrations used here, we do not detect luminescence from aqueous Eu^{3+} ions or species in the growth solution. The absence of luminescence from the growth solution is an advantage in our experiments; only the solid crystals yield detectable signal, and the background is dark.

Experimental Section

Crystal Growth. All crystals were grown at room temperature (22–25 °C) from supersaturated solutions prepared by mixing appropriate amounts of stock solutions consisting of salts ($\text{CaCl}_2 \cdot 2\text{H}_2\text{O}$, $\text{Na}_2\text{C}_2\text{O}_4 \cdot \text{H}_2\text{O}$, and $\text{EuCl}_3 \cdot 6\text{H}_2\text{O}$, Aldrich) dissolved in ultrapure water (18 MΩ cm resistivity). The $\text{Na}_2\text{C}_2\text{O}_4$ stock was typically added to a solution containing CaCl_2 and EuCl_3 to give a growth solution with total $[\text{Ca}^{2+}] = [\text{C}_2\text{O}_4^{2-}] = 4.8 \times 10^{-4}$ mol/L and total $[\text{Eu}^{3+}] = 5 \times 10^{-6}$ mol/L. The ionic strength was approximately 2.0×10^{-2} mol/L. These concentrations were chosen to yield a supersaturated solution near the spontaneous precipitation limit. Higher ionic strengths were not considered in these studies. Adding background electrolyte such as NaCl to increase ionic strength complicates the interpretation of interfacial events, since Na^+ and Cl^- can

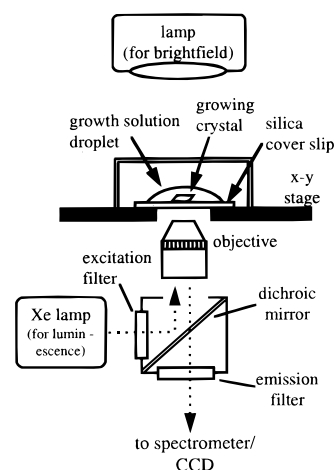


Figure 2. Side-view schematic of luminescence microspectroscopy (LMS) optics and sample stage.

form complexes at crystal surfaces, altering chemistry and charge. Na^+ and Cl^- can also associate with ions in solution, altering supersaturation. We will address higher ionic strengths in future work.

Initial mixing of the batch was with a Teflon coated magnetic stir bar for approximately 30 s. Crystals were then grown under static conditions on silica cover slips in glass crystallizing dishes. To assess the early stages of growth, a drop of the freshly prepared solution was placed on a clean silica cover slip on the microscope stage and growing crystals were viewed from below (Figure 2). In this configuration, crystals were either heterogeneously nucleated at the silica surface or were delivered there by diffusion or gravity after spontaneous nucleation and growth in the bulk.⁸ We monitored crystallization during the intermediate stages of growth, when crystals were between 1 and 30 μm . Specific experimental conditions are discussed in more detail below.

Luminescence Microspectroscopy (LMS). The LMS apparatus in our laboratory shares features with scanning microspectroscopy instruments^{9–13} but is optically simpler in that it uses standard broadband light sources without scanning. It is based on an inverted epifluorescence microscope (Nikon Diaphot) equipped with a 100 W xenon lamp and appropriate optical filters for luminescence measurements and a lamp for standard transmission mode brightfield microscopy (Figure 2). At the output of the microscope is a $1/8$ m spectrometer (Acton SpectraPro) with a liquid nitrogen cooled CCD camera (Princeton Instruments, 512SB). In imaging mode the spectrometer simply serves as a series of mirrors. For spectroscopy, an entrance slit assembly is engaged along with a diffraction grating (1200 groove/mm, 500 nm blaze) that disperses light horizontally on the CCD. A combination of CCD chip binning (software controlled) and $x-y$ sample stage control provides spatially resolved spectroscopy capabilities. Wavelength calibration is with the 546.73 nm mercury plasma line. Data acquisition is performed using commercial software (WinSpec, Princeton Instruments).

A custom optical filter cube (Omega Optical) was designed for europium micro-spectroscopy. The excitation filter/dichroic mirror combination transmits light from 390 to 560 nm. The dichroic mirror reflects these wavelengths and transmits wavelengths > 560 nm. The emission filter is a 590 nm long pass absorption filter. Unfortunately, the excitation/emission filter design in the imaging spectrometer precludes direct observation of the nondegenerate $^5\text{D}_0 \rightarrow ^7\text{F}_0$ band near 580 nm. As discussed below, however, a parallel laser spectroscopy experiment allows

measurement of this important emission band. We also note that the emission filter introduces nonlinearity in the luminescence spectra between 585 and 600 nm. We quantitatively correct for this nonlinearity using the measured transmission of the emission filter.

Raman and Laser Spectroscopies. After removal from the growth solution, crystals grown on the silica cover slip substrates were analyzed using a conventional Raman spectrometer in a grazing angle geometry described previously.¹⁴ The Raman measurements are “blind” relative to the LMS measurements since the Raman signal is detected from unknown scatterers on the surface. Fortunately, for each Raman scatterer we can simultaneously measure the Eu^{3+} luminescence spectrum excited by the 514.5 nm argon laser line. By matching the laser-induced luminescence spectra with those measured in the imaging spectrometer, we can link the Raman spectra with crystal morphology. In addition, the laser spectroscopy measurements provide the $^5\text{D}_0 \rightarrow ^7\text{F}_0$ emission band that is not detectable in the imaging spectrometer.

Environmental Scanning Electron Microscopy (ESEM). ESEM was performed using a Philips-Electroscan ESEM 2020 operating at 12–20 kV and 4–5 Torr.

Results

Eu^{3+} inhibition of CaC_2O_4 Nucleation. Nucleation induction times were assessed for stirred solutions using a custom-built laser light scattering apparatus. The induction time measured was the lag time before a scattering signal was detected. We found that despite large supersaturations, the presence of micromolar quantities of Eu^{3+} significantly inhibited CaC_2O_4 nucleation in stirred solutions. For example, spontaneous precipitation was observed immediately in equimolar solutions with total $[\text{Ca}^{2+}] = [\text{C}_2\text{O}_4^{2-}] = 4.0 \times 10^{-4}$ mol/L in the absence of Eu^{3+} . In the presence of 5×10^{-6} mol/L Eu^{3+} , however, the observed induction time was > 1 h, even with vigorous stirring. Lowering the Eu^{3+} concentration shortened the induction times. Increasing the Eu^{3+} concentration lengthened the induction times, although eventually (e.g., at 5×10^{-5} mol/L Eu^{3+}), $\text{Eu}_2(\text{C}_2\text{O}_4)_3 \cdot x\text{H}_2\text{O}$ crystals precipitate. Eu^{3+} is similar in inhibitory effectiveness to the pyrophosphate and phosphonate anions, well-known inhibitors of calcium oxalate monohydrate nucleation.^{15,16}

These qualitative nucleation observations suggest that Eu^{3+} increases the interfacial free energy of nucleation. Our research seeks to elucidate the molecular mechanisms of this process. As a first step, we explore how Eu^{3+} ions interact with CaC_2O_4 crystals during the early stages of growth.

$\text{Eu}^{3+}:\text{CaC}_2\text{O}_4$ Crystallization. Control experiments were performed in which a supersaturated CaC_2O_4 solution (total $[\text{Ca}^{2+}] = [\text{C}_2\text{O}_4^{2-}] = 4.8 \times 10^{-4}$ mol/L) containing no Eu^{3+} was placed on the silica substrate. Within minutes, large (20–40 μm) platelike polycrystals appeared along with smaller (1–2 μm) prismatic crystals. The former morphology suggests the trihydrate phase of calcium oxalate ($\text{CaC}_2\text{O}_4 \cdot 3\text{H}_2\text{O}$ or COT); the latter suggests the thermodynamically favored calcium oxalate monohydrate ($\text{CaC}_2\text{O}_4 \cdot \text{H}_2\text{O}$ or COM). The appearance of mixed COT and COM phases would be consistent with our high supersaturation sample preparation.¹⁷ No luminescence signal is detectable in these CaC_2O_4 crystals.

When the supersaturated solution described above also contains 5×10^{-6} mol/L EuCl_3 , crystal growth is altered significantly. Several crystal morphologies appear and evolve, including a large fraction of bipyramidal crystals normally

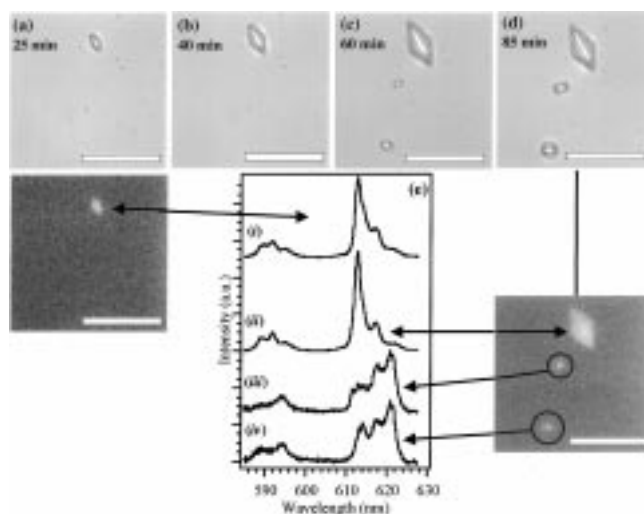


Figure 3. Optical microscopy and LMS measurements during the early stages of growth of $\text{Eu}^{3+}:\text{CaC}_2\text{O}_4$ (growth solution has total $[\text{Ca}^{2+}] = [\text{C}_2\text{O}_4^{2-}] = 4.8 \times 10^{-4}$ mol/L; total $[\text{Eu}^{3+}] = 5 \times 10^{-6}$ mol/L); (a) 4.5 μm crystal after 25 min of growth, luminescence image is directly below; (b) after 40 min of growth; (c) 60 min of growth, including the appearance of new 2 μm crystals; (d) 85 min of growth, the luminescence image is below the brightfield image; (e)(i–iv) luminescence spectra associated with the crystals in (a) and (d), as indicated by arrows. Scale bar = 20 μm .

associated with calcium oxalate dihydrate ($\text{CaC}_2\text{O}_4 \cdot 2\text{H}_2\text{O}$ or COD). All exhibit weak luminescence, indicating that Eu^{3+} is incorporated in the growing crystals.

Figure 3 illustrates our ability to spatially resolve and measure luminescence signal from these micrometer-sized crystals during the early stages of growth. Figures 3a–d show the time sequence of the same surface spot after initial mixing in a typical growth experiment. Figure 3a shows a 4.5 μm crystal observed after 25 min of growth. Directly below Figure 3a is the luminescence image showing the same field of view. The small crystal exhibits weak luminescence. The Eu^{3+} luminescence spectrum from this crystal is provided in Figure 3e(i), as indicated by the arrow. The spectrum features a $^5\text{D}_0 \rightarrow ^7\text{F}_2$ band with a strong component at 612.8 nm and a $^5\text{D}_0 \rightarrow ^7\text{F}_1$ band split into three components centered near 592 nm.

At 40 min (Figure 3b), the crystal has grown and is beginning to show a bipyramidal morphology. This morphology suggests COD, looking at the $\{100\}$ face. At 60 min (Figure 3c) the original crystal is larger and two additional crystals have appeared. These small crystals continue to grow, and Figure 3d shows all three at 85 min of growth. Below Figure 3d is the corresponding luminescence image. Although the printed image contrast is poor, all three of the crystals show luminescence signal. The Eu^{3+} spectrum associated with each of the crystals is provided in Figure 3e(ii–iv). The spectrum associated with the bipyramid (Figure 3e(ii)) is very similar to that measured for the crystal at 25 min (Figure 3e(i)), with the larger crystal showing slightly narrower luminescence bands. The spectra of the late-appearing crystals (iii and iv) are significantly altered with respect to that of the bipyramidal crystal, indicating different Eu^{3+} bonding environments. In particular, the strong feature at 612.8 nm observed in the bipyramidal crystal is much weaker in the small, late appearing crystals, which have strong $^5\text{D}_0 \rightarrow ^7\text{F}_2$ components at 618 and 621 nm. These spectral differences are discussed later.

Figure 4 provides a detailed analysis of the bipyramidal crystals. The crystal shown was grown for 17 h on a silica cover slip and then removed from the growth solution for analysis.

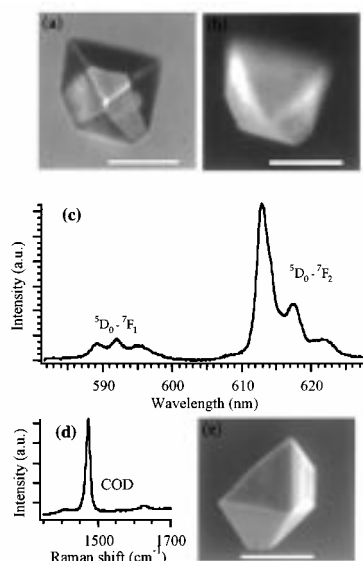


Figure 4. (a) Optical microscope image of bipyramidal crystal after 17 h growth (because these crystals are transparent, reflections make morphology determination difficult in the optical images); (b) luminescence image of crystal in (a); (c) luminescence spectrum from same crystal; (d) representative Raman oxalate $\nu_s(\text{C}-\text{O})$ stretch spectrum, which indicate calcium oxalate dihydrate (COD); (e) ESEM image of a representative bipyramidal crystal showing the characteristic morphology. Scale bars = 20 μm .

Figures 4a and b show the crystal in brightfield and epiluminescence imaging modes. Figure 4c is the spectrum of the $^5\text{D}_0 \rightarrow ^7\text{F}_{1,2}$ luminescence bands measured from this specific crystal. The $^5\text{D}_0 \rightarrow ^7\text{F}_{3,4}$ bands were also measured but are not shown. We augmented the imaging spectrometer measurements by placing the sample in a Raman spectrometer with 514.5 nm argon beam excitation. By rastering the cover slip through the laser beam, we were able to locate crystals exhibiting laser-induced Eu^{3+} luminescence spectra matching those observed in the imaging spectrometer. This links the Raman spectrum to the crystal morphology. Raman signal in the oxalate $\nu_s(\text{C}-\text{O})$ stretch region is shown in Figure 4d. The strong singlet observed at 1475 cm^{-1} is the Raman signature for COD.¹⁴ The Raman measurements thus confirm the dihydrate phase suggested by the bipyramidal crystal morphology. Figure 4e provides an ESEM image of a representative bipyramidal crystal. The crystals show truncated edges where they grow against the cover slip. Note that incorporation of Eu^{3+} in the COD crystals does not alter the known COD morphology, and smooth faces are observed. Crystal like that in Figure 4 are referred to here as Eu:COD.

Similar analyses were performed for the other crystal morphologies observed in the experiments. Representative ESEM images of the ill-formed morphologies are shown in Figure 5 along with their corresponding luminescence spectra. These spectra are higher intensity versions of those observed for the late-appearing crystals in Figure 3. Two strong features are observed in the $^5\text{D}_0 \rightarrow ^7\text{F}_1$ band at 588.7 and 594.5 nm. The $^5\text{D}_0 \rightarrow ^7\text{F}_2$ band shows three strong features at 613.8, 617.4, and 621.3 nm, which vary in relative intensity for the different crystals. All of the crystals exhibiting the luminescence spectra of Figure 5 show the Raman spectrum of COM, as shown in Figure 5d. These crystals are referred to as Eu:COM.

Although a transient COT phase cannot be ruled out in the $\text{Eu}^{3+}:\text{CaC}_2\text{O}_4$ experiments, our Raman measurements only show evidence of the COM and COD phases. Previous rare earth-calcium oxalate coprecipitation studies¹⁸ also showed no evidence of COT coprecipitation.

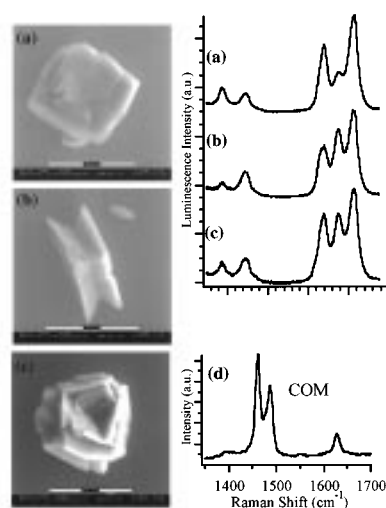


Figure 5. (a-c) ESEM images of CaC_2O_4 crystal morphologies and their associated luminescence spectra; (d) representative Raman oxalate $\nu_s(\text{C}-\text{O})$ stretch spectrum, which suggests calcium oxalate monohydrate (COM); all luminescence spectra like those in a-c show the Raman spectrum in d. Scale bars = 15 μm .

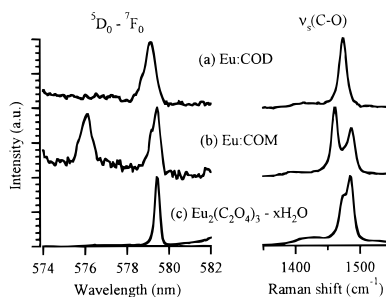


Figure 6. Detail of the $^5\text{D}_0 \rightarrow ^7\text{F}_0$ luminescence bands and the oxalate $\nu_s(\text{C}-\text{O})$ stretch region (Raman) for different crystals ($\lambda_{\text{ex}} = 514.5 \text{ nm}$); (a) Eu:COD crystals, such as in Figure 4; (b) Eu:COM crystals, such as in Figure 5; (c) $\text{Eu}_2(\text{C}_2\text{O}_4)_3 \cdot x\text{H}_2\text{O}$.

Figure 6 shows detail of the $^5\text{D}_0 \rightarrow ^7\text{F}_0$ bands of the different $\text{Eu}^{3+}:\text{CaC}_2\text{O}_4$ crystals and their corresponding Raman spectra. Also included are the $^5\text{D}_0 \rightarrow ^7\text{F}_0$ band and the oxalate $\nu_s(\text{C}-\text{O})$ Raman stretch spectrum for $\text{Eu}_2(\text{C}_2\text{O}_4)_3 \cdot x\text{H}_2\text{O}$ for comparison. The Eu:COD $^5\text{D}_0 \rightarrow ^7\text{F}_0$ spectrum shows a single feature centered at 579.1 nm with evidence of a high energy shoulder. The band is approximately twice as broad as the corresponding $\text{Eu}_2(\text{C}_2\text{O}_4)_3 \cdot x\text{H}_2\text{O}$ spectrum, suggesting a distribution of Eu^{3+} binding sites. The Eu:COM spectrum shows a feature at 579.5 nm (red shifted relative to the Eu:COD peak) as well as an additional high energy feature at 576.1 nm.

Stirred solution experiments were also performed. Unlike the static samples, stirring led to the precipitation of CaC_2O_4 crystals with no incorporated Eu^{3+} detectable by luminescence. Instead, a large fraction of small CaC_2O_4 crystallites formed, accompanied by a small fraction of Eu^{3+} -containing amorphous material. Contact nucleation during stirring mechanically increases the number density of embryonic nuclei in the system. We believe the trace quantities of Eu^{3+} in these systems are not sufficient to yield detectable incorporation in this large number of crystallites.

Discussion

The techniques and results presented above represent a new approach for investigating interfacial crystallization phenomena in real time. By utilizing the spatial resolution of an optical microscope, we were able to select micrometer-scale crystals

for spectral analysis. Subsequently linking these spectra with Raman spectroscopy measurements allowed us to establish a link between observed crystal morphology, phase, and admixture ion bonding environments. Here we interpret the incorporation of Eu^{3+} in CaC_2O_4 crystals in terms of crystal lattice models.

Properties of Eu^{3+} make it an outstanding probe of admixture effects on calcium crystal formation. Eu^{3+} and Ca^{2+} have similar ionic radii and coordination properties,⁵ and both form bonds with oxygen ligands that are primarily ionic in character. Trivalent Eu^{3+} , however, creates a charged defect when substituting for divalent Ca^{2+} . Differences in the ionic equilibrium properties of Ca^{2+} and Eu^{3+} should also be considered. Eu^{3+} hydrolyzes water more effectively, is more strongly hydrated, and forms more stable complexes with both OH^- and $\text{C}_2\text{O}_4^{2-}$.^{19,20}

The inhibitory effect of trace metal ions on ionic crystal growth is well established and has been linked to the large dehydration energy and low dehydration frequency of the impurity metal.^{21,22} The fact that Eu^{3+} ions are strongly hydrated in aqueous solution is thus consistent with their inhibitory behavior in our experiments. It is reasonable to conclude that a partially hydrated Eu^{3+} ion or complex strongly adsorbs at active growth sites, inhibiting growth. Strong adsorption is inferred from the fact that Eu^{3+} exhibits high affinity for oxalate anions²⁰ and forms stable, inner-sphere complexes in solution. We also observe strong $^5\text{D}_0 \rightarrow ^7\text{F}_2$ emission bands in our LMS experiments, indicating that the Eu^{3+} site symmetry has been broken, most likely by replacing one or more coordinating waters with an anionic ligand at the surface. Subsequent incorporation of the adsorbed Eu^{3+} ion into the growing oxalate crystal is difficult since it requires further dehydration. The LMS results provide insight into the structural aspects of this process for different CaC_2O_4 hydrates.

Two classes of $\text{Eu}^{3+}:\text{CaC}_2\text{O}_4$ crystals were observed in our experiments: $\text{Eu}:\text{COD}$ (Figure 4) and $\text{Eu}:\text{COM}$ (Figure 5). Stabilization of the higher hydrate (COD) is consistent with the hydrated nature of lighter lanthanide oxalates, which occur as oxalate decahydrates (e.g., $\text{Eu}_2(\text{C}_2\text{O}_4)_3 \cdot 10\text{H}_2\text{O}$).^{23–26} Given the well-developed morphologies and smooth faces of the $\text{Eu}:\text{COD}$ crystals (Figure 4), we infer that Eu^{3+} is incorporated into COD without significantly disrupting the COD lattice. Earlier radiotracer studies have also shown that Eu^{3+} forms mixed crystals with COD.¹⁸ We believe successful incorporation of Eu^{3+} is potentially related to the nature of the waters of hydration in COD. X-ray crystallography of COD has suggested that in addition to the two waters of hydration, zeolitic water is present up to a fraction of 0.5 per unit cell.^{27,28} Ca^{2+} ions in COD are coordinated by eight oxygens (two water and six oxalate oxygens).²⁷ Eu^{3+} at a Ca^{2+} lattice site could have its excess positive charge compensated by an OH^- anion in the zeolitic water space.

The ill-formed nature of the $\text{Eu}:\text{COM}$ crystals (Figure 5) suggest that Eu^{3+} incorporation is not as compatible with COM as it was with COD. The fact that COM is a lower hydrate is consistent with this observation. As discussed above, Eu^{3+} forms highly hydrated oxalates. For Eu^{3+} to be incorporated at a Ca^{2+} lattice site the ion must be almost completely dehydrated, since Ca^{2+} in COM is coordinated by only one water oxygen. Alternatively, partially dehydrated Eu^{3+} ions or complexes may adsorb to COM surfaces, inhibiting growth. Subsequent overgrowth does not appear to involve simple incorporation of Eu^{3+} into Ca^{2+} lattice sites. This is consistent with radiotracer studies

that have suggested that Eu^{3+} follows a Freundlich adsorption isotherm when interacting with COM and does not form mixed crystals.¹⁸

The Eu^{3+} spectra provide insight into the Eu^{3+} bonding environments in the $\text{Eu}:\text{COM}$ crystals. Most striking is the fact that the $^5\text{D}_0 \rightarrow ^7\text{F}_0$ spectra (Figure 6b) show that there are two classes of bonding sites in the COM crystals. The first class is characterized by a $^5\text{D}_0 \rightarrow ^7\text{F}_0$ band centered at 579.5 nm. The second class has an unusually high energy $^5\text{D}_0 \rightarrow ^7\text{F}_0$ band centered at 576.1 nm. The $^5\text{D}_0 \rightarrow ^7\text{F}_1$ and $^5\text{D}_0 \rightarrow ^7\text{F}_2$ bands of the $\text{Eu}:\text{COM}$ crystals (Figure 5) showed variations in relative intensities that likely correspond to different occupancies of the two classes of sites. The $\text{Eu}:\text{COM}$ $^5\text{D}_0 \rightarrow ^7\text{F}_0$ band at 579.5 nm coincides with the $^5\text{D}_0 \rightarrow ^7\text{F}_0$ band in $\text{Eu}_2(\text{C}_2\text{O}_4)_3 \cdot x\text{H}_2\text{O}$ (Figure 6c). This first class of Eu^{3+} spectra likely represents specifically adsorbed europium oxalate complexes.

The second class of sites, with the $^5\text{D}_0 \rightarrow ^7\text{F}_0$ band at 576.1 nm, is more difficult to interpret. This is an unusually high energy $^5\text{D}_0 \rightarrow ^7\text{F}_0$ band for a Eu^{3+} ion coordinated by oxygens, and suggests a high crystal field strength, ionic bonding environment.³⁰ High energy $^5\text{D}_0 \rightarrow ^7\text{F}_0$ bands have also been observed in Eu^{3+} -doped oxyapatite crystals,³¹ where an oxygen anion residing in a channel in the apatite structure closely coordinates Eu^{3+} , leading to the strong crystal field. Similar arguments can be made here. It is conceivable that a fraction of Eu^{3+} ions enter the COM lattice along with a charge compensating, closely coordinated anion such as OH^- . The COM unit cell has two crystallographically distinct Ca^{2+} sites.³² A distinguishing feature of the two closely related Ca^{2+} sites is that one has a closely coordinated water (bond length $\text{Ca}-\text{O}(\text{H}_2\text{O}) = 2.398(4) \text{ \AA}$), the other has a more distant water ($\text{Ca}-\text{O}(\text{H}_2\text{O}) = 2.541(4) \text{ \AA}$).³² Again, we can speculate that Eu^{3+} may be incorporated along with a closely coordinated, charge, compensating anion such as OH^- . If the anion substitutes for the water ligand in COM, however, the Eu^{3+} ion must be completely dehydrated to reside in a Ca^{2+} lattice site. We note here that anhydrous $\text{La}_2(\text{C}_2\text{O}_4)_3$ is amorphous,²³ which is consistent with the ill-formed crystal morphologies.

More experiments will greatly enhance our interpretation. We are currently conducting atomic force microscope studies of the CaC_2O_4 crystal growth in the presence of Eu^{3+} admixtures. We are also pursuing face-specific LMS studies on larger $\text{Eu}:\text{CaC}_2\text{O}_4$ crystals. Those measurements will provide more detailed growth surface structure information, which has been shown to be critical to trace element incorporation in minerals.^{33,34} Improved Eu^{3+} spectroscopy experiments include luminescence lifetime measurements to provide a measure of Eu^{3+} hydration⁷ and low-temperature site-selective laser spectroscopy to distinguish Eu^{3+} sites within the ensemble.

Conclusions

In situ, spatially resolved Eu^{3+} luminescence spectra were collected for different CaC_2O_4 crystal morphologies during the early stages of growth using luminescence microspectroscopy (LMS). By combining LMS results with laser-induced luminescence and Raman spectroscopies, a relationship between Eu^{3+} local structure, CaC_2O_4 phase, and crystal morphology was established. Eu^{3+} stabilizes the dihydrate phase of CaC_2O_4 and appears to occupy Ca^{2+} lattice sites, resulting in the faceted, bipyramidal crystals associated with $\text{CaC}_2\text{O}_4 \cdot 2\text{H}_2\text{O}$. The thermodynamically favored monohydrate phase also appears during growth. In these crystals, however, Eu^{3+} leads to ill-formed $\text{CaC}_2\text{O}_4 \cdot \text{H}_2\text{O}$ crystal morphologies and is not readily incorporated into the crystal lattice. Two classes of Eu^{3+} bonding sites

were observed in the monohydrate, one likely consisting of specifically adsorbed europium oxalate complexes, the other possibly Eu^{3+} in a Ca^{2+} lattice site. This illustrates how the LMS technique can be applied to analyze single-crystal growth processes in real time.

Acknowledgment. This work was performed as part of M.J.L.'s postdoctoral research at the University of Washington Department of Bioengineering. We thank Gretchen Baneyx for her contributions to the imaging spectrometer development, Chester Gall for his aid in measuring induction times for stirred solutions, Kim Trabbic for her assistance with the Raman measurements, and Professor Paul Yager for use of the Raman spectrometer. The authors gratefully acknowledge fruitful discussions with Dr. Shelli (Letellier) Dennis (UW) and Dr. Allison A. Campbell (Pacific Northwest National Laboratory). Funding was provided by the Battelle Pacific Northwest National Laboratory, the National Institutes of Health (Grant GM49063), and the National Science Foundation through the University of Washington Engineered Biomaterials (UWEB) Engineering Research Center. L.T. acknowledges support from a NIH Molecular Biophysics Training Grant.

References and Notes

- (1) Myerson, A. S. *Handbook of Industrial Crystallization*; Butterworth-Heinemann: Boston, 1993.
- (2) Lowenstam, H. A.; Weiner, S. *On Biomineralization*; Oxford: New York, 1989.
- (3) Finlayson, B. *Kidney Int.* **1978**, *13*, 344.
- (4) Franceschi, V. R.; Horner, H. T., Jr. *Botanical Rev.* **1980**, *46*, 361.
- (5) Bünzli, J.-C. G.; Choppin, G. R. *Lanthanide Probes in the Life, Chemical, and Earth Sciences: Theory and Practice*; Elsevier: New York, 1989; Chapter 7.
- (6) Ryabchikov, D. I.; Ryabukhin, V. A. *Analytical Chemistry of Yttrium and the Lanthanide Elements*; Ann Arbor-Humphrey: Ann Arbor, 1970; p 50.
- (7) Horrocks, W. DeW., Jr.; Sudnick, D. R. *J. Am. Chem. Soc.* **1979**, *101*, 334.
- (8) Rieke, P. C. *Mater. Sci. Eng. C* **1995**, *C2*, 181.
- (9) Delahaye, M.; Dhamelincourt, P. *J. Raman Spectrosc.* **1975**, *3*, 33.
- (10) Rosasco, G. J.; Etz, E. S.; Cassatt, W. A. *Appl. Spectrosc.* **1975**, *29*, 396.
- (11) Zhang, H.; Föhlisch, A.; Kunz, C.; Moewes, A.; Pretorius, M.; Ranck, A.; Sievers, H.; Storzjohann, I.; Wedemeier, V.; Voss, J. *Rev. Sci. Instrum.* **1995**, *66*, 3513.
- (12) Feofanov, A.; Sharonov, S.; Valisa, P.; Da Silva, E.; Nabiev, I.; Manfait, M. *Rev. Sci. Instrum.* **1995**, *66*, 3146.
- (13) LaPlant, F.; Ben-Amotz, D. *Rev. Sci. Instrum.* **1995**, *66*, 3537.
- (14) Letellier, S. R.; Lochhead, M. J.; Campbell, A. A.; Vogel, V. *Biochim. Biophys. Acta* **1998**, *1380*, 31.
- (15) Nancollas, G. H.; Gardner, G. L. *J. Cryst. Growth* **1974**, *21*, 267.
- (16) Gardner, G. L. *J. Phys. Chem.* **1978**, *82*, 864.
- (17) Brečević, L.; Kralj, D.; Garside, J. *J. Cryst. Growth* **1989**, *90*, 460.
- (18) Purkayastha, B. C.; Bhattacharyya, S. N. *J. Inorg. Nucl. Chem.* **1959**, *10*, 103.
- (19) Rard, J. A. *Chem. Rev.* **1985**, *85*, 555.
- (20) Manning, P. G. *Can. J. Chem.* **1966**, *44*, 3057.
- (21) Hottenhuis, M. H. J.; Lucasius, C. B. *J. Cryst. Growth* **1986**, *78*, 379.
- (22) Reddy, M. M.; Nancollas, G. H. *J. Cryst. Growth* **1976**, *35*, 33.
- (23) Gilpin, V.; McCrone, W. C. *Anal. Chem.* **1952**, *24*, 225.
- (24) Jenkins, I. L.; Moore, F. H.; Waterman, M. J. *J. Inorg. Nucl. Chem.* **1965**, *27*, 77.
- (25) Ivanov, V. I. *Russ. J. Inorg. Chem.* **1970**, *15*, 16.
- (26) Morris, D. E.; Hobart, D. E. *J. Raman Spectrosc.* **1988**, *19*, 231.
- (27) Tazzoli, V.; Domeneghetti, A. *Mineral.* **1980**, *65*, 327.
- (28) Sterling, C. *Acta Crystallogr.* **1965**, *18*, 917.
- (29) Albin, M.; Horrocks, W. DeW., Jr. *Inorg. Chem.* **1985**, *24*, 895.
- (30) Lochhead, M. J.; Bray, K. L. *Phys. Rev. B* **1995**, *52*, 15763.
- (31) Piriou, B.; Fahmi, D.; Dexpert-Ghys, J.; Taitai, A.; Lacout, J. L. *J. Lumin.* **1987**, *39*, 97.
- (32) Deganello, S.; Piro, O. E. *N. Jb. Miner. Mh.* **1981**, *H2*, 81.
- (33) Northrup, P. A.; Reeder, R. J. *Am. Mineral.* **1994**, *79*, 1167.
- (34) Rokovan, J.; Reeder, R. J. *Am. Mineral.* **1994**, *79*, 892.